

Article

Experimental Investigation of Solid Rocket Scramjet Based on Central Strut

Jia Zeng *, Guohui Wang, Hui Huang, Jian Fan and Haosu Wang

Beijing Institute of Astronautical Systems Engineering, Beijing 100076, China

* Correspondence: zengjia_fat@163.com

Abstract: Scramjet based on solid propellant has become a potential choice for the development of future hypersonic vehicles. In this paper, a boron-containing solid rocket scramjet based on the central strut injection was proposed, and the ground direct-connect experiment with the equivalence ratios of 0.43 to 2.4 under the flight condition of Mach 6, 25 km was carried out. The pressure and flow rate over time were measured in the experiment. The results show that the engine can realize stable supersonic mode or subsonic mode combustion by changing the gas flow rate. The engine can effectively increase the combustor pressure, reduce the unstable combustion time, and advance the strong combustion position by increasing the gas flow rate. The engine achieved high combustion efficiency when the equivalence ratio was about 1, with a maximum of 88.28%. A numerical simulation analysis was also carried out in this paper. Compared to the experimental results, the pressure error obtained by numerical simulation was less than 4%, and the typical position error was less than 3%, suggesting that the simulation model can be used to predict the behavior of scramjet.

Keywords: solid rocket scramjet; direct-connect test; central strut injection; numerical simulation; boron-containing propellant



Citation: Zeng, J.; Wang, G.; Huang, H.; Fan, J.; Wang, H. Experimental Investigation of Solid Rocket Scramjet Based on Central Strut. *Aerospace* **2024**, *11*, 410. <https://doi.org/10.3390/aerospace11050410>

Academic Editor: Sebastian Karl

Received: 26 March 2024

Revised: 1 May 2024

Accepted: 6 May 2024

Published: 19 May 2024



Copyright: © 2024 by the authors. Licensee MDPI, Basel, Switzerland. This article is an open access article distributed under the terms and conditions of the Creative Commons Attribution (CC BY) license (<https://creativecommons.org/licenses/by/4.0/>).

1. Introduction

Scramjet, as a new type of high-speed propulsion, has become the focus of research. Currently, most of the research is based on liquid fuels such as liquid hydrogen and kerosene [1–4]. However, the inherent deficiencies of liquid fuel in storage, maintenance, acceleration, stable combustion, rapid response, and technical complexity also bring restrictions to the application of liquid scramjet [5–8]. The solid rocket scramjet uses a gas generator to produce fuel-rich primary gas and organizes the mixing combustion of the primary gas and incoming air in the combustor [9]. In contrast, the air-breathing propulsion system with a solid propellant has the inherent advantages of high energy density, good flame stability, strong acceleration ability, excellent storage performance, and high rapid response ability [10,11], providing another potential choice for the development of future hypersonic vehicles.

Boron, as a solid fuel additive, has extremely high-density specific impulse and heat value [12,13]. However, in the application of solid scramjet, the combustion efficiency of boron particles is greatly limited due to the very short residence time in the combustor [14–16]. Therefore, how to improve the residence time and mixing efficiency of boron particles, improve the combustion efficiency, and release more combustion enthalpy in a finite scale have become the focus of current research [17–20]. Lv Z et al. [21] proposed a scheme of a solid rocket scramjet with side and nose intakes and conducted direct-connect experimental studies, validating the feasibility of the solid rocket gas scramjet. Li et al. [22] proposed a flame stabilization scheme for a solid rocket scramjet based on a cavity and strut, which was experimentally proven to be feasible; however, it caused a large ablation and total pressure loss. Liu et al. [23] attempted a new combustion organization scheme combining cavity and pneumatic slope to enhance the combustion efficiency of a boron-containing

propellant solid rocket scramjet, and the combustion performance has proved to be optimized via the enlarged low-speed area near the cavity and the strengthened particles reflux. Huang et al. [24] investigated the influence of the cavity and its position on the performance; results show that the cavity can significantly improve combustion efficiency, and the effect of the cavity location on performance is related to particle distribution. Yang et al. [25,26] proposed a modular solid scramjet combustor with a Symmetrical Structure and improved the mixing and combustion of the fuel-rich mixture by the narrow/lobe cavity.

The above work has shown that the cavity can effectively enhance the mixing and combustion of primary gas in the solid scramjet. However, most of them were focused on the side wall injection form, which injects the fuel-rich primary gas into the combustor from the inner wall position and enhances the mixing by adjusting the injection angle or adopting different cavity structures. There are some problems in this injection form, such as the large total pressure loss, uneven combustion heat release, and easy ablation of the cavity [27–29]. Therefore, in this paper, a new scheme of solid rocket scramjet based on the central strut injection was proposed, and the ground experiment and numerical simulation with different equivalence ratios under the flight condition of Mach 6, 25 km were carried out. The pressure distribution and performance of the combustor were obtained through experiment and simulation, which verified the rationality and advantages of the scheme and analyzed the influence of the equivalence ratio on combustion characteristics and performance. Several helpful conclusions are drawn to provide a basis for further study.

2. Materials and Methods

2.1. Experiment Setup

The direct-connect experimental system consists of an incoming flow simulation system and the experimental engine. The function of the incoming flow simulation system is to provide the engine with incoming flow simulating conditions of inlet exit, and its schematic is shown in Figure 1. The tank provides a certain flow of air for the system. The air is heated in the heater through the combustion of gas oxygen and alcohol and is supplemented with a certain flow of oxygen in the mixer to make the flow rate, total temperature, total pressure, and oxygen content of the simulated air consistent with the actual air at specific altitude and Mach number conditions. The simulated air finally enters the combustor through the facility nozzle, which ensures that the Mach number of the airflow entering the engine is consistent with the actual inlet exit and makes the airflow parameters evenly distributed in the axial section. In order to verify the accuracy of simulation parameters, several measurement points are set in the stabilizer and nozzle.

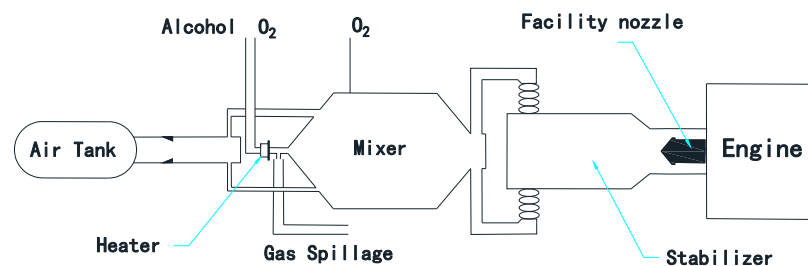


Figure 1. Schematic of the incoming flow simulation system.

The schematic of boron-containing solid rocket scramjet based on central strut injection is shown in Figure 2, which is mainly composed of gas generator, isolator, central strut, combustor, and powder igniter. The strut is placed in the center of the channel. The working process of the engine is as follows: the igniter ignites the boron-containing propellant grain in the gas generator, and the generated fuel-rich primary gas is ejected from the central strut at the rear of the isolator. And the high-speed simulated incoming flow enters the combustor on both sides of the channel after passing through the isolator. The primary gas and incoming air with the same flow direction are mixed and burned in the combustor,

forming a thermal blockage, and finally discharged through the expansion nozzle to generate thrust.

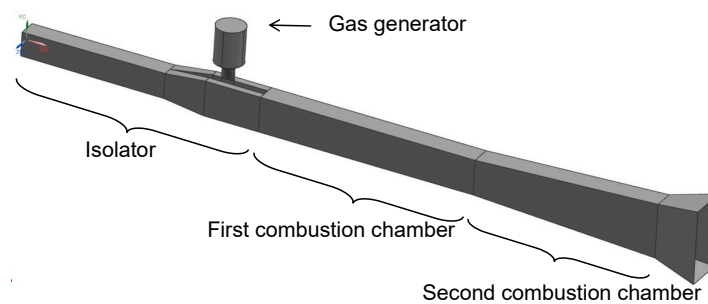


Figure 2. Schematic of the solid rocket scramjet.

The section of the engine is square, and the geometric design of the typical position is obtained by solving with the theory of one-dimensional analysis of scramjet. The combustor is divided into two stages, and the combustion basically occurs in the first combustor. The gas generator adopts an end-burning structure form, using boron-based fuel-rich solid propellant. The schematic of the central strut injection is shown in Figure 3. Primary gas enters the combustor at supersonic speed after passing through the Laval nozzle at the strut exit, and the direction was consistent with the airflow.

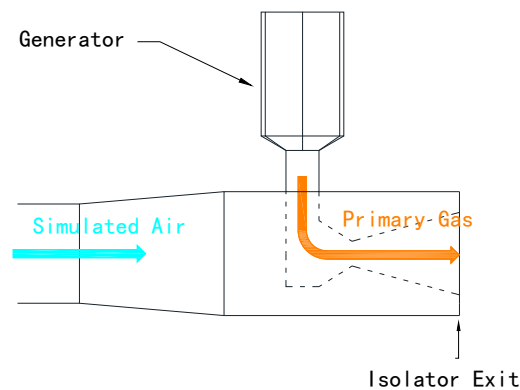


Figure 3. Schematic of the central strut injection.

2.2. Experimental Conditions

The combustion organization and combustion boundary experiments were carried out under Mach 6.0 and 25 km flight conditions for the central strut solid rocket scramjet. The corresponding simulation inlet parameters of the engine are shown in Table 1, and the experimental conditions are shown in Table 2, with the equivalence ratio ranging from 0.41 to 2.4. The experiments mainly measured the wall pressure of the engine along the channel with 67 measuring points. The engine performance is calculated based on the measured wall pressure. The data measuring system is based on VXI bus technology, which monitors the operation status of each device by collecting data in real time.

Table 1. Parameters of the simulated air.

Flight Mach Number	Flight Height (km)	Static Pressure (Pa)	Mass Flow Rate (kg/s)	Mass Fraction of O ₂
6.0	25.0	2549	2.5	0.23

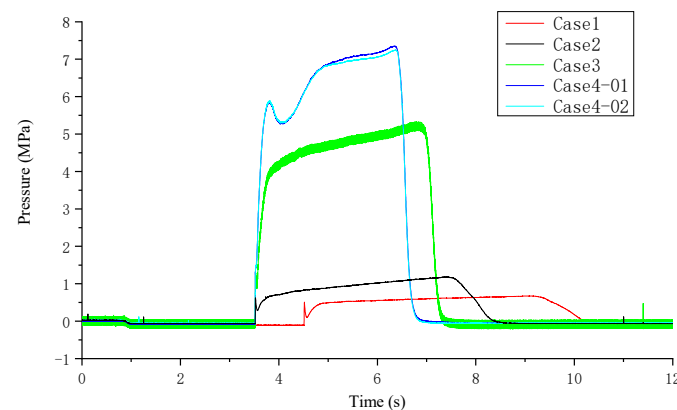
Table 2. Experimental conditions.

Cases	Equivalence Ratio
1	0.41
2	0.53
3	1.06
4	2.49

3. Results and Discussion

3.1. Working Characteristics of the Gas Generator

The function of the gas generator is to provide fuel-rich primary gas for the scramjet and inject it into the combustor for secondary combustion according to the specified pressure, temperature, flow, injection speed, and injection angle. The control of the gas flow rate was realized by adjusting the throat area and the number of gas generators. Figure 4 shows the pressure–time curve of the gas generators during four experiments.

**Figure 4.** Evolution of pressure of the gas generator.

It can be seen that the pressure continued to increase during operation, with a maximum increase of 29.5%. The shape of the end-burning propellant grain is a flat cylinder with a diameter of 180 mm and a height of 30 mm, which may lead to the edge combustion effect. The burning rate of propellant at the edge of the grain is significantly higher than that at the center of the grain, which makes the grain form a conical burning feature. This will lead to an increase in propellant combustion surface area and gas generator combustor pressure so that the gas flow also continues to increase. For example, the equivalence ratio in case 3 increased from 0.99 to 1.11 over time.

3.2. Combustion Characteristics When the Equivalence Ratio Was 1

Figures 5 and 6 show the variation of wall pressure over time in the isolator and the combustor during the case 3 experiment, respectively. In these figures, two red curves correspond to the right axis, representing the pressure of the heater and gas generator, respectively. The gas generator started ignition after the heater pressure became stable during the experiment. Other curves of different colors represent the pressure of measuring points at various relative axial positions. The entire engine testing process has two key moments:

1. Heater ignition start: In the first second of the experiment, the heater ignition started, and the pressure of the heater rapidly rose and reached a stable state. At the same time, the pressure at the measuring points rapidly increased to a steady state, almost synchronously increasing with the pressure of the heater, without any significant delay.
2. Gas generator ignition start: At 3.5 seconds, the ignition system issued an ignition command, and the gas generator ignited to a start. About 0.3 s after the ignition signal was sent, the gas generator entered a stable combustion state, and the engine ignited

successfully. As time went on, the pressure of the gas generator continued to rise, and the gas flow rate gradually increased until it ended at the seventh second of operation.

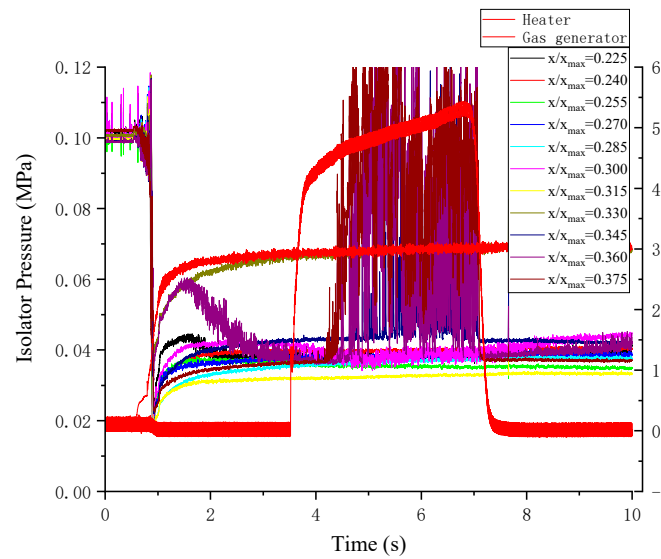


Figure 5. Evolution of wall pressure in the isolator in case 3.

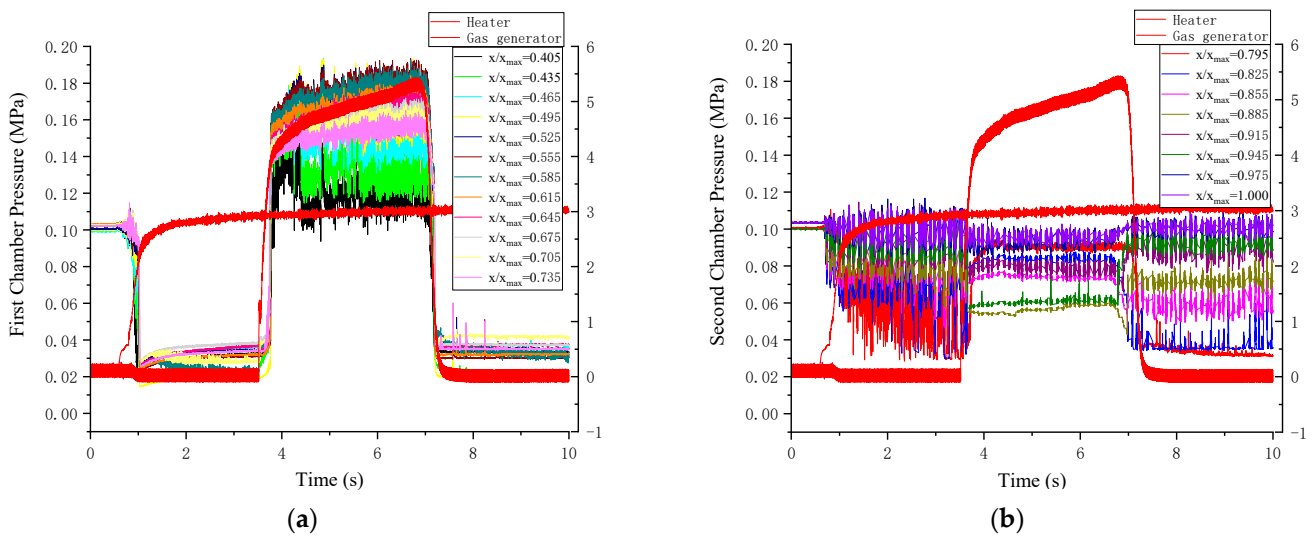


Figure 6. Evolution of wall pressure in case 3 in (a) the first combustor and (b) the second combustor.

As shown in Figure 5, the pressure upstream of the isolator remained stable throughout the entire process, unaffected by combustion backpressure. The pressure at the three downstream measuring points exhibited a significant increase after the ignition of the gas generator, accompanied by amplitude fluctuations of no less than 0.08 MPa. This indicated that the pre-combustion shock wave generated by combustion backpressure had propagated to these positions. The variations in pressure at these three points did not synchronize with the initiation of the gas generator. The delay times at the three locations were 0.55, 0.75, and 1.31 s, respectively, reflecting the process of the pre-combustion shock wave propagating upstream. The forward propagation speed of the wave within the isolator gradually decreased, maintaining a range between 107 mm/s and 300 mm/s. In addition, instability in the flow field behind the shock wave was observed, manifested as significant low-frequency oscillations in the pressure measurements at the post-shock wave location. This pre-combustion shock wave propagation is attributed to the combined

effects of the combustion generation process and the intensification of combustion due to the increase in the flow rate of the gas generator.

In Figure 6, the increase in pressure in the combustor was almost synchronized with the ignition and start-up of the gas generator, which was caused by the backward-to-forward generation process of engine combustion. The maximum pressure occurred at the position $x/x_{\max} = 0.555$. It is noteworthy that between $t = 3.75$ s and 4.63 s, the pressure in the combustor showed a trend of first rising and then decreasing, especially near the upstream measuring points. After $t = 4.63$ s, the pressure at all measuring points tended to stabilize, and the combustor reached a stable combustion state. Therefore, there was no significant delay (<0.2 s) in the ignition process of the engine, but it took about 0.9 s to establish a stable combustion state, while it took about 0.5 s in case 4. The pressure at the measuring points in the second combustor decreased significantly, indicating that the engine experienced a thermal choke at the transition between the two combustors. The pressure at each measuring point remained stable, with little impact from the change of the gas flow, indicating that there was no significant combustion reaction in the second combustor, and the heat release occurred primarily in the first combustor.

In order to better understand the combustion process and combustion characteristics of the engine, Figure 7 shows the pressure distribution along the wall surface of the engine at several typical moments. These moments correspond to different states during the combustion process. Before ignition ($t = 3$ s) and after the end of combustion ($t = 8$ s), the pressure distribution exhibited typical characteristics of unheated variable cross-section pipe flow. The reflection of the waves in the first combustor caused the pressure along the way to be stable but accompanied by fluctuations. In the second combustor, the over-expanded flow established a steady back pressure shock after the third measuring point ($x/x_{\max} = 0.806$) to match the ambient atmospheric pressure at the outlet of the engine.

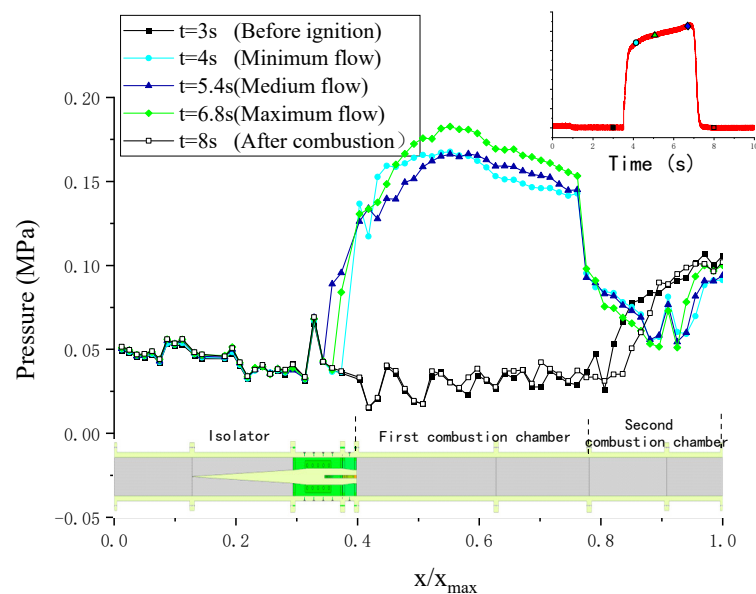


Figure 7. The pressure distribution along the wall surface at several moments.

The engine entered the stable operation phase after $t = 4$ s. At the end of the isolator, the pressure rose sharply, indicating that the gas was burning violently in the combustor, and a pre-combustion shock wave matching the combustion back pressure was established in the isolator. The shock wave moved back and forth slightly over time, with a moving range of about 120 mm and a speed of about 100 mm/s. A sharp drop in pressure caused by thermal choke at the tail of the first combustor ($x/x_{\max} = 0.765$) can be clearly visible in the figure. The subsonic combustion characteristics of the engine were obvious, and the first combustor showed a high combustion pressure ratio and a plump pressure curve, indicating that the engine achieved stable combustion in the subsonic mode.

3.3. Effect Analysis of Equivalence Ratio

The combustion characteristics for various equivalence ratios are further discussed in this section. Figure 8 shows the comparison of pressure distribution along the wall surface for various equivalence ratios. In case 1 and case 2, it can be seen that the pressure was significantly lower than that in case 3 and case 4. During the operation of the engine, the pressure in the upstream combustor basically did not increase, indicating that no combustion reaction occurred in the front section of the first combustor. The pressure in the downstream combustor increased in a fluctuating manner, which was consistent with the basic characteristics of supersonic combustion. The pressure in the combustion zone was obviously affected by the equivalence ratio. The increase in gas flow significantly increased the pressure in the combustor, and the combustion reaction was enhanced. In general, the pressure in the primary combustor was stable and the supersonic characteristics were obvious, so the engine worked in the supersonic combustion mode under the current working condition.

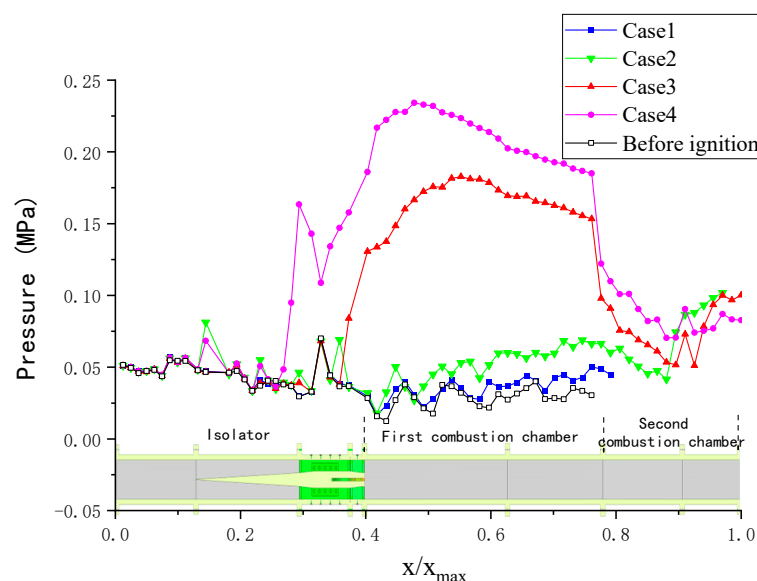


Figure 8. The pressure distribution along the wall surface for various equivalence ratios.

In case 3 and case 4, the engine worked in the subsonic combustion mode. The pressure distribution trends of the two cases were consistent. As the equivalence ratio increased in case 4, the pressure of the combustor rose, and the position of the pre-combustion shock wave moved forward. It is found that the position of the highest pressure in case 4 was closer to the injection position, indicating that the engine was able to achieve a match state of a pre-combustion shock wave, sudden expansion of the flow channel, and initial mixing over a shorter length. In conclusion, the engine can achieve stable subsonic combustion mode when the equivalence ratio is greater than 1, and the increase in fuel flow rate can effectively improve the thrust performance of the engine and advance the strong combustion position.

3.4. Analysis of Combustion Efficiency

The aerodynamic parameters of the thermal throat section can be calculated by linearly fitting the pressure data of the measuring points in the stable combustion area of the first combustor with the least square method and combining it with the flow formula. The flow formula is as follows:

$$q_m = \frac{Kq_{(\lambda)} P^* A}{\sqrt{T^*}} = \frac{0.95 \times Kq_{(1)} P^* A}{\sqrt{T^*}} \quad (1)$$

$$q(\lambda) = \left(\frac{k+1}{2}\right)^{\frac{1}{k-1}} \lambda \left(1 - \frac{k-1}{k+1} \lambda^2\right)^{\frac{1}{k-1}} \quad (2)$$

$$K = \sqrt{\frac{k}{R} \left(\frac{2}{k+1}\right)^{\frac{k+1}{k-1}}} \quad (3)$$

where q_m is the mass flow, P^* is the total pressure, A is the cross-sectional area of the pipe, T^* is the total temperature, $q(\lambda)$ is the dense flow function defined by the velocity coefficient and the specific heat ratio k . R is the universal gas constant, and 0.95 is the area correction coefficient obtained from previous experimental experience, which is used to correct the nonuniformity of the velocity coefficient of the combustor section and the influence of the boundary layer thickness on the reduction of the effective area.

The specific heat ratio k and theoretical total temperature T_{CEA}^* of combustion components under the current working condition of the engine are obtained from the thermal calculation software CEA [30]. The parameters, such as flow rate, pressure at measuring points, and total temperature, are further obtained through mass conservation, and then the combustion efficiency of the thermal throat position of the engine can be obtained through Formula (4).

$$\eta = \frac{(q_1 + q_2) \times T^* - q_1 \times T_{air} - 0.5 \times q_2 \times 300}{(q_1 + q_2) \times T_{CEA}^* - q_1 \times T_{air} - 0.5 \times q_2 \times 300} \quad (4)$$

where q_1 is the total air intake, q_2 is the flow of combustible gas, and 0.5 represents the correction parameter of specific heat capacity at low temperatures (the value is between 0 and 1, which has little effect on the actual calculation).

Affected by the performance characteristics of the gas generator, the equivalence ratio of the engine changed continuously during operation. Export parameters and combustion efficiency at the moments of maximum, medium, and minimum flow rate in case 3 and case 4 were carried out according to the working state of the gas generator. The results are shown in Table 3.

Table 3. Export parameters and combustion efficiency of the first combustor.

Parameters	Case 3			Case 4		
Equivalence Ratio	0.99	1.08	1.11	2.29	2.57	2.64
Pressure (MPa)	0.139	0.145	0.149	0.171	0.178	0.182
Total Pressure (MPa)	0.241	0.252	0.259	0.297	0.309	0.316
Total Temperature (K)	2675.4	2878.4	2998.7	3077.5	3110.7	3119.1
Combustion Efficiency	71.0%	81.7%	88.3%	54.1%	46.4%	45.7%

It can be seen that by increasing the equivalence ratio from 0.5 to 1, the engine can change into a stable subsonic combustion mode, and the combustion performance can be substantially improved. With the equivalence ratio increasing above 2, the performance parameters such as pressure and total temperature continued to increase, while the combustion efficiency was reduced significantly. In addition, it is also found that in case 3, with the improvement in gas flow, the combustion efficiency increased from 70.98% to 88.28%, while it decreased from 54.11% to 45.73% in case 4, which indicated that excessive fuel (equivalence ratio much greater than 1) cannot effectively improve the performance of the combustor.

3.5. Numerical Simulation Analysis

The results of the direct-connect experiment verified the rationality of the theoretical design and the central strut injection scheme of the engine. Compared to the experiment, the numerical simulation can obtain the flow and combustion details of the engine and provide a reference for engine optimization. Therefore, the numerical simulation of the two-phase turbulent combustion of the scramjet was further studied in this paper.

In this paper, the finite volume method was used to discretize the 3D Reynolds-averaged Navier–Stokes equation, and the SST k - ϵ two-equation model was adopted for turbulence enclosure. The convection term was discrete by the second-order upwind difference scheme and the diffusion term by the second-order center difference scheme.

The primary gas component is obtained by thermal calculation. By ignoring the inert components and selecting the main gaseous components for simplified replacement, the alternative components used in the simulation model were finally formed, as shown in Table 4. The inlet of the primary gas was set as the mass flow inlet condition. The B and C particles were described by the DPM model, and their injection direction and position were consistent with that of the primary gas. The particle sizes of B and C were set to 3 μm and 1 μm , respectively [31]. The stochastic tracking approach was used for simulating the trajectories of particles in a turbulent current.

Table 4. Components of the primary gas.

Component	H ₂ (Gas)	CO (Gas)	B (Solid)	C (Solid)	Inert Gas
Mass fraction	5.03%	24.52%	25.27%	9.10%	36.08%

In this paper, a turbulent boundary layer is formed on the surface of solid particles, and a turbulent diffusion flame is formed within the boundary layer. The main combustion mode in the engine is turbulent diffusion combustion, with the reaction rate controlled by the gas diffusion process. Therefore, the turbulent combustion model applies the finite-rate/eddy-dissipation model, which simultaneously calculates the Arrhenius rate and the eddy dissipation rate and uses the smaller value of the two. Due to the high boiling point of B particle, its combustion belongs to the surface combustion mode, which is simplified as a one-step reaction model, and the combustion rate is controlled by the diffusion process and the surface kinetic rate. The boron particles adopt an ignition and combustion model based on the PSU model, and specific parameter settings are detailed in the reference [32].

The grid independence analysis by wall static pressure distributions of the combustor was carried out at first. The coarse grid has about 1.58 million cells, and the medium and fine grids have about 2.75 and 4.84 million cells, respectively. The result is given in Figure 9. In contrast, the results of the medium grid and the fine grid were almost the same, while those for the coarse grid were slightly different. Considering the computational accuracy and the cost, the medium grid is enough for numerical simulation.

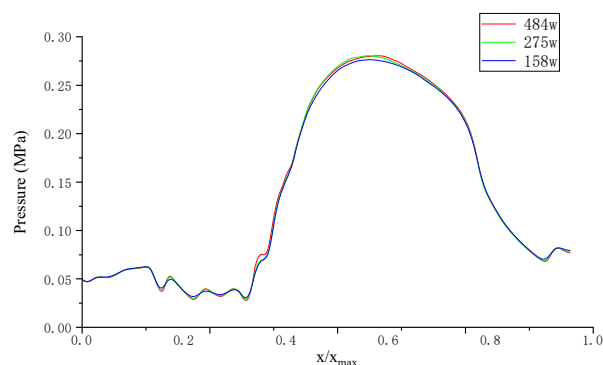


Figure 9. Grid independence analysis.

The case 3 and case 4 experiments were simulated using the numerical method described in this paper. Figure 10 shows the comparison of experimental and numerical pressure distributions along the engine. It can be seen that the pressure distribution obtained from the numerical calculation is in good agreement with the direct-connect experiment data. The predicted error of the pressure is less than 4%, and the maximum pressure point, the starting point of the isolator pressure rise, and the point of sudden

pressure drop in the combustor (thermal throat) of the two cases are accurately reproduced. The axial position error is less than 3%. This indicates that the numerical simulation method used in this article has high accuracy and reliability.

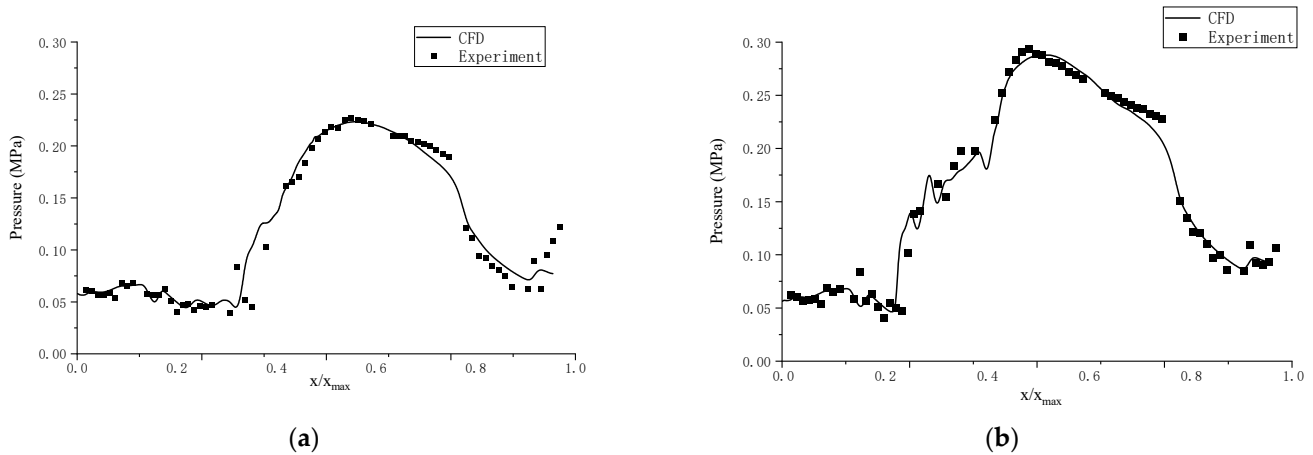


Figure 10. Comparison of experimental and numerical pressure distributions along the engine in (a) case 3 and (b) case 4.

Figure 11 shows the comparison of the average combustion efficiency of each fuel component in different axial sections of the combustor when the equivalent ratio was 1. The combustion efficiency of the gas phase was calculated to be 99.4%, and the combustion efficiency of the B and C were 59.0% and 84.9%, respectively. It can be seen that the combustion efficiency of the gas phase exceeded 90% before the relative axial position reached 25%, indicating that the chemical reaction of the gas phase is strong and mainly concentrated upstream of the combustor. However, the combustion of solid particles lagged behind, indicating that the solid fuels require longer mixing and combustion distances, which was due to the high density and low shear mixing efficiency of solid particles. Therefore, the mixing and combustion efficiency of solid particles at a limited distance was lower than that of gaseous fuel, which may limit the performance of the engine.

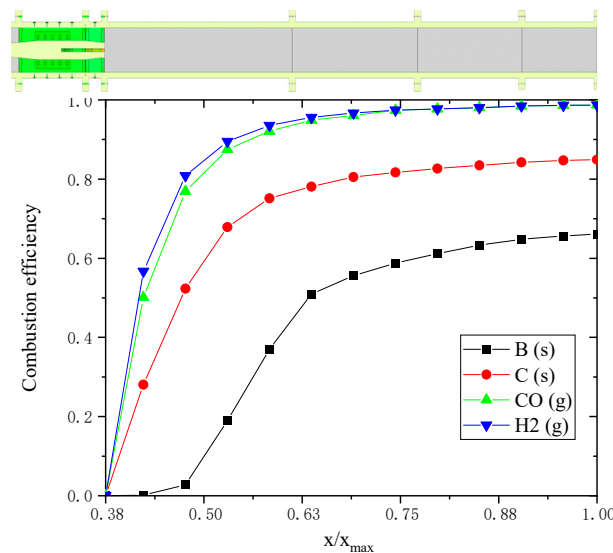


Figure 11. Average combustion efficiency in each axial section of combustor.

4. Conclusions

In this paper, a boron-containing solid rocket scramjet based on central strut injection is proposed, and a direct-connect experiment with the equivalence ratios of 0.43 to 2.4 under the flight condition of Mach 6, 25 km was carried out. The pressure and flow rate

over time were measured in the experiment to obtain the combustion characteristics and performance of the scramjet. The main conclusions are summarized as follows:

1. The boron-containing scramjet based on central strut injection realized supersonic combustion mode when the equivalence ratio was much less than 1 and subsonic combustion mode when the equivalence ratio was greater than 1.
2. The fuel-rich gas mass flow and the pressure of the gas generator continued to increase during the experiment due to the edge-burning effect of the propellant.
3. The engine achieved high combustion efficiency when the equivalence ratio was about 1, with a maximum of 88.28%. With the increase in equivalence ratio, the pressure of the combustor increased continuously, and the combustion efficiency first increased and then decreased.
4. The trend of numerical pressure distributions was consistent with that of the experiment, with a pressure error of less than 4% and a typical position error of less than 3%.

As mentioned above, the scramjet scheme in this paper can achieve stable combustion at a low equivalence ratio and realize the combustion mode transition by changing the equivalence ratio. The strut itself can be used as an ignition and flame retention device, and the downstream injection mode can avoid momentum loss. The ignition delay time of the combustor was less than 0.2 s when the equivalence ratio was 1.06, accompanied by a significant pressure peak, which took about 0.9 s to establish a stable combustion state. As the equivalence ratio increased to 2.49, the duration of the ignition peak reduced to 0.4 s, and the combustion efficiency significantly decreased. The numerical results show that low combustion efficiency of particles is still the key factor limiting engine performance. Our future work will focus on optimizing the structural parameters of solid scramjet engines and the combustion efficiency of condensed phase particles, and the reliable numerical simulation method can provide a foundation for the study.

Author Contributions: Conceptualization, J.Z.; methodology, J.Z.; validation, H.H. and G.W.; formal analysis, G.W.; investigation, G.W.; resources, H.W.; data curation, J.Z.; writing—original draft preparation, J.Z.; writing—review and editing, H.W.; visualization, H.H.; supervision, J.F.; project administration, J.F. All authors have read and agreed to the published version of the manuscript.

Funding: This research received no external funding.

Data Availability Statement: Additional data may be made available by contacting the corresponding author.

Acknowledgments: The authors appreciate the valuable comments on the paper by the reviewers.

Conflicts of Interest: The authors declare no conflicts of interest.

References

1. Betelin, V.; Kushnirenko, A.; Smirnov, N.; Nikitin, V.; Tyurenkova, V.; Stomov, L. Numerical investigations of hybrid rocket engines. *Acta Astronaut.* **2018**, *144*, 363–370. [[CrossRef](#)]
2. Choubey, G.; Yuvarajan, D.; Huang, W.; Shafee, A.; Pandey, K. Recent research progress on transverse injection technique for scramjet applications—a brief review. *Int. J. Hydrogen Energy* **2020**, *45*, 27806–27827. [[CrossRef](#)]
3. Das, N.; Pandey, K.; Sharma, K. A brief review on the recent advancement in the field of jet engine-scramjet engine. *Mater. Today Proc.* **2021**, *45*, 6857–6863. [[CrossRef](#)]
4. Meng, Y.; Sun, W.; Gu, H.; Chen, F.; Zhou, R. Supersonic Combustion Mode Analysis of a Cavity Based Scramjet. *Aerospace* **2022**, *9*, 826. [[CrossRef](#)]
5. Nithish Reddy, P.; Venkatasubbaiah, K. Numerical investigations on development of scramjet combustor. *J. Aerosp. Eng.* **2015**, *28*, 04014120. [[CrossRef](#)]
6. He, Z.; Wang, H.; Li, F.; Tian, Y.; Wan, M.; Zhu, J. Effect of Fuel-Injection Distance and Cavity Rear-Wall Height on the Flameholding Characteristics in a Mach 2.52 Supersonic Flow. *Aerospace* **2022**, *9*, 566. [[CrossRef](#)]
7. Zhu, S.-H.; Xu, X. Experimental study on flame transition in a two-stage struts dual-mode scramjet. *J. Aerosp. Eng.* **2017**, *30*, 06017002. [[CrossRef](#)]
8. Mohammad, A.K.; Sumeray, C.; Richmond, M.; Hinshelwood, J.; Ghosh, A. Assessing the sustainability of liquid hydrogen for future hypersonic aerospace flight. *Aerospace* **2022**, *9*, 801. [[CrossRef](#)]

9. Chi, H.-W.; Wei, Z.-J.; Wang, L.-H.; Li, B.; Wu, Z.-W. Numerical investigation of self-ignition characteristics of solid-fuel scramjet combustor. *J. Propuls. Power* **2015**, *31*, 1019–1032. [[CrossRef](#)]
10. He, Y.; Chen, Y.; Liu, D.; Liu, J.; Lai, M.; Liang, X. Research on solid rocket/scramjet combined engine. In Proceedings of the 21st AIAA International Space Planes and Hypersonics Technologies Conference, Xiamen, China, 6–9 March 2017; p. 2390.
11. Zhang, H.; Wang, N.; Wu, Z.; Fang, G.; Wei, Z. Preliminary investigation of paraffin-based fuel combustion in solid fuel scramjet. *Acta Astronaut.* **2020**, *173*, 119–130. [[CrossRef](#)]
12. Mandal, S.; Hashim, S.A.; Roy, A.; Karmakar, S. A short review of challenges and prospects of boron-laden solid fuels for ramjet applications. *FirePhysChem* **2023**, *3*, 179–200. [[CrossRef](#)]
13. Yang, L.; Yonggang, G.; Lei, S.; Zexin, C.; Xiaojing, Y. Preliminary experimental study on solid rocket fuel gas scramjet. *Acta Astronaut.* **2018**, *153*, 146–153. [[CrossRef](#)]
14. Gany, A. Comprehensive consideration of boron combustion in airbreathing propulsion. In Proceedings of the 42nd AIAA/ASME/SAE/ASEE Joint Propulsion Conference & Exhibit, Sacramento, CA, USA, 9–12 July 2006; p. 4567.
15. Gany, A. Thermodynamic limitation on boron energy realization in ramjet propulsion. *Acta Astronaut.* **2014**, *98*, 128–132. [[CrossRef](#)]
16. Kadosh, H.; Natan, B. Internal ballistics of a boron-containing solid fuel ramjet. *Combust. Sci. Technol.* **2021**, *193*, 2672–2691. [[CrossRef](#)]
17. Liu, L.-L.; He, G.-Q.; Wang, Y.-H. Effect of oxidizer on the combustion performance of boron-based fuel-rich propellant. *J. Propuls. Power* **2014**, *30*, 285–289. [[CrossRef](#)]
18. Li, C.; Zhao, X.; Xia, Z.; Ma, L.; Chen, B. Influence of the vortex generator on the performance of solid rocket scramjet combustor. *Acta Astronaut.* **2019**, *164*, 174–183. [[CrossRef](#)]
19. Bao, H.; Zhou, J.; Pan, Y. Effect of cavity configuration on kerosene spark ignition in a scramjet combustor at Ma 4.5 flight condition. *Acta Astronaut.* **2015**, *117*, 368–375. [[CrossRef](#)]
20. Cai, Z.; Wang, T.; Sun, M. Review of cavity ignition in supersonic flows. *Acta Astronaut.* **2019**, *165*, 268–286. [[CrossRef](#)]
21. Lv, Z.; Xia, Z.-X.; Liu, B.; Liu, Y.-C. Experimental and numerical investigation of a solid-fuel rocket scramjet combustor. *J. Propuls. Power* **2016**, *32*, 273–278. [[CrossRef](#)]
22. Li, C.; Xia, Z.; Ma, L.; Zhao, X.; Chen, B. Experimental and numerical study of solid rocket scramjet combustor equipped with combined cavity and strut device. *Acta Astronaut.* **2019**, *162*, 145–154. [[CrossRef](#)]
23. Liu, J.; Wang, N.-F.; Wang, J.; Li, Z.-Y. Optimizing combustion performance in a solid rocket scramjet engine. *Aerosp. Sci. Technol.* **2020**, *99*, 105560. [[CrossRef](#)]
24. Huang, H.; Feng, Z.; Ma, L.; Yang, T.; Li, C. Numerical research on the performance of solid fuel rocket scramjet combustor. *Proc. Inst. Mech. Eng. Part G J. Aerosp. Eng.* **2022**, *236*, 1450–1461. [[CrossRef](#)]
25. Yang, P.; Xia, Z.; Ma, L.; Chen, B.; Feng, Y.; Li, C.; Zhao, L. Influence of the multicavity shape on the solid scramjet. *Int. J. Aerosp. Eng.* **2021**, *2021*, 1–14. [[CrossRef](#)]
26. Yang, P.; Xia, Z.; Ma, L.; Chen, B.; Feng, Y.; Li, C.; Zhao, L. Direct-connect test of solid scramjet with symmetrical structure. *Energies* **2021**, *14*, 5589. [[CrossRef](#)]
27. Kummitha, O.R.; Suneetha, L.; Pandey, K. Numerical analysis of scramjet combustor with innovative strut and fuel injection techniques. *Int. J. Hydrogen Energy* **2017**, *42*, 10524–10535. [[CrossRef](#)]
28. Wang, L.; Wu, Z.; Chi, H.; Liu, C.; Tao, H.; Wang, Q. Numerical and experimental study on the solid-fuel scramjet combustor. *J. Propuls. Power* **2015**, *31*, 685–693. [[CrossRef](#)]
29. Wang, L.; Chi, H.; Liu, C.; Tao, H.; Wang, Q. Numerical and Experimental study on the Solid Fuel Scramjet Combustor with a cavity flame holder. In Proceedings of the 50th AIAA/ASME/SAE/ASEE Joint Propulsion Conference, Cleveland, OH, USA, 28–30 July 2014; p. 3453.
30. Gordon, S.; McBride, B.J. *Computer Program for Calculation of Complex Chemical Equilibrium Compositions and Applications. Part 1: Analysis*; NASA Center for Aerospace Information (CASI): Linthicum, MD, USA, 1994.
31. Wang, Z.-H.; Wang, Y.-X.; Kang, J.-F.; Chen, L.-Q.; Zhang, S.-Y. Design and experimental study on sampling in secondary combustion of solid rocket ramjet. *J. Solid Rocket. Technol.* **2012**, *35*, 769–772.
32. Chen, B.; Xia, Z.; Huang, L.; Hu, J. Ignition and combustion model of a single boron particle. *Fuel Process. Technol.* **2017**, *165*, 34–43. [[CrossRef](#)]

Disclaimer/Publisher’s Note: The statements, opinions and data contained in all publications are solely those of the individual author(s) and contributor(s) and not of MDPI and/or the editor(s). MDPI and/or the editor(s) disclaim responsibility for any injury to people or property resulting from any ideas, methods, instructions or products referred to in the content.